THE IMPLEMENTATION AND NUMERICAL ANALYSIS OF FULLY-COUPLED NON-ISOTHERMAL FLUID FLOW THROUGH A DEFORMABLE POROUS MEDIUM

Justin Pogacnik[1], Peter Leary[1], and Peter Malin[1]

[1]Institute for Earth Science and Engineering, University of Auckland, 58 Symonds St. Floor 6, Auckland, New Zealand

j.pogacnik@auckland.ac.nz

Keywords: *Fully coupled finite element model, deformable porous media, geothermal systems, heat and mass transfer, power-law scaling.*

ABSTRACT

This work seeks to simulate subsurface fluid flow and heat transport within a deformable porous medium. Previous work indicates that it is imperative to consider the *in situ* spatial fluctuations recorded in well-log and well-core data to achieve accurate numerical flow simulations for non-deforming porous solids. The consideration of *in situ* spatial property fluctuations naturally gives rise to preferential pathways of fluid flow and heat transport. Provision for solid deformations offers a logical step forward to allow for stress-controlled fluctuation evolution of *in situ* properties. A sophisticated numerical model will be able to capture the growth and collapse of *in situ* voids, fractures, and fracture connectivity due to variation in fluid pressure and flow, faulting, and temperature as, say, induced at Enhanced/Engineered Geothermal System (EGS) projects.

The relevant linear momentum, mass, and enthalpy balance equations have been coupled in a combined finite element and finite difference analysis. The governing differential equations and discretized set of equations are realized in preliminary results for 2D vertical planes in which one or more horizontal wellbores act as flow sources/sinks. The model presented in this work is a critical first step toward full 3D EGS heat exchange reservoir development and fluid flow simulation.

1. INTRODUCTION

Traditionally, the true spatial variations of porosity and permeability are ignored in favor of their mean values (e.g., Sutter et al., 2011). However, previous work indicates that it is imperative to consider true spatial fluctuations in 'poroperm' properties. Leary and Walter (2008) show that observed tight gas well production unpredictability is traceable to the false assumption that *in situ* flow in gas sands is quasi-uniform rather than spatially fluctuating. On an economic note, Goldstein et al (2011) cite "insufficiently predictable reliability of geothermal reservoir performance (and in particular, the [un]predictable reliability of EGS reservoirs)" that is traceable to EGS models based on quasi-uniform media.

Quasi-uniform media are effectively assumed to have a 'white noise' Fourier power-spectra in spatial frequency k,

$$S(k) \sim const.$$

Microresistivity and most other geophysical well-log data have, however, Fourier power-spectra that scale inversely with wave number by

$$S(k) \sim \frac{1}{k}$$

over about 5 decades of the length scale from 10^{-2}m to 10^{3}m. The specific well log properties that obey this law include: sonic wave speeds, electrical resistivity, soluble chemical species density, neutron porosity, and mass density. Also, via fracture-connectivity percolation, clastic rock well-core data show a close spatial fluctuation relationship between well-core permeability κ and well-core porosity n

$$\delta n \sim \delta \log(\kappa)$$

that governs how permeability spatially varies *in situ*.

This work simulates subsurface fluid flow and heat transport within a 2-D deformable porous medium with power-law scaling fluctuations in porosity combined with the aforementioned relationship controlling permeability. Few available finite element codes are equipped to handle the full spatial variability in porosity and permeability that are necessary to accurately depict the physics of *in situ* flow and heat transport. Further, the codes that can handle this behavior do not solve for the fully coupled problem, but only consider fluid and thermal flow through non-deformable media. Therefore, a new finite element code was written in C++ that is capable of modeling the above-mentioned scenario.

Section 2 details the boundary value problem and the governing coupled differential equations for the linear momentum balance, mass balance, and enthalpy balance. In Section 3, the finite element method is applied to yield a discretized linear system of equations where the unknowns are nodal values for solid displacements, pore fluid pressures, and temperatures. Section 4 outlines a benchmark problem and a specific trial numerical analysis for a 2D vertical section consisting of two horizontal wellbores cycling water in/out of an EGS volume. Section 5 provides discussion of the preliminary results and the future work that is being undertaken for this analysis.

2. GOVERNING EQUATIONS

2.1 Linear Momentum Balance

A suitable first step in acquiring the finite element system of equations is to consider the linear momentum balance:

$$\underline{\nabla} \cdot \underline{\underline{\sigma}} + \rho \underline{g} = \underline{0}$$

where $\underline{\nabla} \cdot$ refers to the gradient operator, $\underline{\underline{\sigma}}$ is the Cauchy stress tensor, $\underline{g}$ is the gravity acceleration vector, and ρ is the average density of the entire matrix:

$$\rho = (1-n)\rho^s + n\rho^w,$$

where ρ^s is the density of the solid grains, ρ^w is the density of the fluid (water) surrounding the grains, and n is the porosity defined as the volume of void space per unit volume. The Cauchy stress can be expressed as a vector and split into two components, the effective stress component $\underline{\sigma}''$ and a pore pressure component as

$$\underline{\sigma} = \underline{\sigma}'' + \alpha \underline{\underline{m}} p,$$

where α is a dimensionless constant between 0 and 1, $\underline{\underline{m}}$ is related to the identity tensor, and p is the pore fluid pressure (Lewis and Schrefler 1998; Ingebritsen, Sanford, and Neuzil 2006). Assuming linear isotropic elastic behavior, the effective stress is calculated as

$$\underline{\sigma}'' = \underline{\underline{D}}_e \left(\underline{\varepsilon} - \underline{\varepsilon}_T \right),$$

where $\underline{\underline{D}}_e$ is the standard elasticity tensor, $\underline{\varepsilon}$ is the mechanical strain vector, and $\underline{\varepsilon}_T$ is the thermal strain vector. In the effective stress equation,

$$\underline{\varepsilon} = \underline{\underline{L}}\,\underline{u}$$

and

$$\underline{\varepsilon}_T = \underline{m}\left(\beta_s / 3\right) T$$

where $\underline{\underline{L}}$ is a matrix of spatial derivatives, $\underline{u}$ is the displacement vector, $\underline{\mathrm{m}}$ again is related to the identity matrix, β_s is the coefficient of thermal expansion of the solid matrix, and T is the temperature.

2.2 Mass Balance

Consideration of both the fluid and solid mass balance equations gives:

$$0 = -\left((1-n)\beta_s + n\beta_w\right)\frac{\partial T}{\partial t} + \left(\frac{1-n}{K_s} + \frac{n}{K_w}\right)\frac{\partial p}{\partial t} + \underline{\nabla}\cdot\underline{v}^s + \underline{\nabla}\cdot\left\{\frac{\underline{\underline{\kappa}}}{\mu_w}\left[-\underline{\nabla}p + \rho g\right]\right\} - Q_p$$

where S_w is the fluid saturation and has been omitted for the fully saturated case, $\underline{v}_s$ is the solid matrix velocity from the system elastic modulus, $\underline{\underline{\kappa}}$ is the permeability matrix, and Q_p is fluid flow into the system.

2.3 Enthalpy Balance

Lastly, to fully couple thermal effects, we consider the enthalpy balance equation:

$$\left(\rho_w C_w + C_s \rho_s\right)\frac{\partial T}{\partial t} + \rho^w C_w \frac{\underline{\underline{\kappa}}}{\mu_w}\left(-\underline{\nabla}P + \rho\underline{g}\right)\cdot\underline{\nabla}T - \underline{\nabla}\cdot\left\{\underline{\underline{\chi}}\cdot\underline{\nabla}T\right\} = 0$$

where C_w is the specific heat of the fluid, C_s is the specific heat of the solid grains, and $\underline{\underline{\chi}}$ is related to the diffusivity of the medium.

The thermal properties of solid and fluid are taken to be constant in space and time with the exception of fluid density, which has standard linearized temperature dependence. The assumption of constant fluid viscosity is disputable. In these simulations, the fluid viscosity for water at 200°C was used (Table 1). The possibility exists to incorporate temperature-dependent spatial variations in fluid viscosity into the code (Figure 15). This is the subject of future work. Compared with spatial variation in fracture density and poroperm properties documented by well-log and well core data to vary significantly on all scale lengths, the thermal properties of rock constituents vary little in value and have few observable constraints to enter into the model equations.

3. THE FINITE ELEMENT METHOD

3.1 Boundary Value Problem

Figure 1 depicts an arbitrary 2-D porous domain Ω with a boundary Γ that is subject to natural and essential boundary conditions on portions of Γ denoted Γ_h and Γ_g, respectively. Natural boundary conditions enforce forces on the system, such as external tractions, mass fluid flow, or temperature fluxes. Essential boundary conditions enforce known degrees of freedom, such as solid displacements, pore fluid pressures, and temperature. The domain is considered to be a fully saturated assemblage of rigid solid grains bonded by weak cements and having a spatially fluctuating density of fluid-filled void space between grains. Void space fluids percolate between voids where grain-grain cement bonds are ruptured by tectonically imposed finite-strain of the bulk medium. The controlling physical variable is grain-scale fracture density. At a critical density of grain-scale fractures, long-range spatial correlations between grain-scale fractures arise, creating the observed power-law scaling properties of well log spatial fluctuations (Leary 2002).

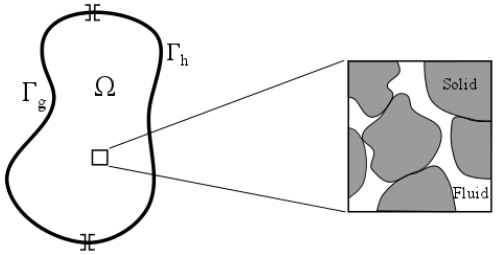

Figure 1: An arbitrary porous domain.

The solid-fluid matrix is non-isothermal and grain assemblages are subject to small strains on all scale lengths. Therefore, the problem is evaluated as a coupled problem

involving temperature and fluid flow through a deformable porous medium.

3.2 Discretization and Solution

The first step in the application of the Finite Element Method (FEM) is to define the approximation spaces for the nodal values of the unknowns: displacement, pressure, and temperature. These functions are defined by:

$$\underline{u}^* = \underline{\underline{N}}_u \underline{u}$$

$$p^* = \underline{N}_p \underline{p}$$

$$T^* = \underline{N}_T \underline{T}$$

where (.)* represents the exact solution of the unknowns, the N_* are the finite element shape functions that are a vector in the case of the scalar unknowns and a 2nd order tensor in the case of the vector unknown (displacement). The vectors $\underline{u}$, $\underline{p}$, and $\underline{T}$ are the finite element approximations to the exact solutions. The shape functions are not necessarily the same order. There is evidence reported in the literature that higher order shape functions are required for the displacement degrees of freedom in the undrained limit state. This is called a "mixed method" and requires elements that satisfy the Babuska-Brezzi convergence criterion. Elements that use second-order interpolation functions for displacement degrees of freedom and first-order interpolation functions for pressure and temperature degrees of freedom satisfy this condition. These elements were implemented and used in this work. Each quadrilateral element contains 4 nodes for representing pressure and temperature degrees of freedom, but nine nodes to represent displacement degrees of freedom. The main advantage of mixed method elements reported by Lewis and Schrefler (1998) and Aboustit (1985) is a significant decrease in pressure field oscillations. The results reported in Section 4 utilize higher order mixed elements.

Introducing the standard finite element discretization gives rise to the global system of equations to be solved:

$$\underline{\underline{K}}\underline{u} - \underline{\underline{K}}_{tt}\underline{T} - \underline{\underline{Q}}\underline{p} = \underline{f}_u$$

$$\underline{\underline{H}}\underline{P} + \underline{\underline{Q}}^T \frac{\partial \underline{u}}{\partial t} + \underline{\underline{S}}\frac{\partial \underline{P}}{\partial t} + \underline{\underline{R}}\frac{\partial \underline{T}}{\partial t} = \underline{f}_p$$

and

$$\underline{\underline{C}}_t \frac{\partial \underline{T}}{\partial t} + \underline{\underline{K}}_t \underline{T} = \underline{f}_t$$

where:

$$\underline{\underline{K}} = \int_\Omega \underline{\underline{B}}^T \underline{\underline{D}}_e \underline{\underline{B}} d\Omega$$

$$\underline{\underline{K}}_{tt} = \int_\Omega \underline{\underline{B}}^T \underline{\underline{D}}_e \underline{m} \frac{\beta_s}{3} \underline{N}_T \, d\Omega$$

$$\underline{\underline{Q}} = \int_\Omega \underline{\underline{B}}^T \alpha \underline{m} \underline{N}_p \, d\Omega$$

$$\underline{\underline{H}} = \int_\Omega \left(\nabla \underline{N}_p\right)^T \frac{\underline{\underline{\kappa}}}{\mu_w} \left(\nabla \underline{N}_p\right) d\Omega$$

$$\underline{\underline{S}} = \int_\Omega \underline{N}_p^T \left(\frac{1-n}{K_s} + \frac{n}{K_w}\right) \underline{N}_T d\Omega$$

$$\underline{\underline{R}} = \int_\Omega \underline{N}_p^T \left((n-1)\beta_s - n\beta_w\right) \underline{N}_T d\Omega$$

$$\underline{\underline{C}}_t = \int_\Omega \underline{N}_T^T \left(\rho_w C_w + C_s \rho_s\right) \underline{N}_T d\Omega$$

$$\underline{\underline{K}}_t = \int_\Omega \underline{N}_T^T \rho_w C_w \frac{\underline{\underline{\kappa}}}{\mu_w} \left(-\nabla \underline{N}_p \underline{P} + p_w \underline{g}\right) \cdot \nabla \underline{N}_T \, d\Omega + \int_\Omega \left(\nabla \underline{N}_T\right)^T \cdot \left\{\underline{\underline{\chi}} \cdot \nabla \underline{N}_T\right\} d\Omega$$

$$\underline{f}_u = \int_\Omega \underline{\underline{N}}_u^T \rho \underline{g} d\Omega + \int_\Gamma \underline{\underline{N}}_u^T \underline{t} \, d\Gamma$$

$$\underline{f}_p = \int_\Omega \left(\nabla \underline{N}_p\right)^T \frac{\underline{\underline{\kappa}}}{\mu_w} \rho \underline{g} \, d\Omega - \underline{q}_{out} + \underline{Q}_{in}$$

$$\underline{f}_t = \int_\Gamma \left[\underline{N}_T^T \underline{\underline{\chi}} \cdot \nabla \underline{N}_T\right] \cdot \underline{n} \, d\Gamma + \underline{q}(T^* - T)$$

Where

$$\underline{\underline{\chi}} = \rho_w C_w \left[n\sigma_s + (1-n)\sigma_w\right] \underline{\underline{I}}$$

is the diffusivity tensor with solid and fluid diffusivities and $\underline{\underline{I}}$ is the identity tensor. The matrices $\underline{\underline{B}}$, N_*, and $\underline{\underline{D}}_e$ are standard matrices used in finite elements. Their exact structure can be found in Lewis and Schrefler (1998) or Hughes (2000). The values of Young's modulus, Poisson's ratio (both in $\underline{\underline{D}}_e$), β_s, ρ_s, ρ_w, S_w, n, C_s, C_w, σ_s, σ_w, μ_w, and $\underline{\underline{\kappa}}$ are material input parameters.

$\underline{\underline{K}}_t$ introduces a nonlinearity into the system of equations that must be solved using an appropriate technique, such as the Newton-Raphson iteration scheme. The final matrix system of equations that is solved can be constructed as:

$$\begin{bmatrix} \underline{\underline{K}} & -\underline{\underline{Q}} & \underline{\underline{K}}_{tt} \\ \underline{\underline{0}} & \underline{\underline{H}} & \underline{\underline{0}} \\ \underline{\underline{0}} & \underline{\underline{0}} & \underline{\underline{K}}_t \end{bmatrix} \begin{Bmatrix} \underline{u} \\ \underline{p} \\ \underline{T} \end{Bmatrix} + \begin{bmatrix} \underline{\underline{0}} & \underline{\underline{0}} & \underline{\underline{0}} \\ \underline{\underline{Q}}^T & \underline{\underline{S}} & \underline{\underline{R}} \\ \underline{\underline{0}} & \underline{\underline{0}} & \underline{\underline{C}}_t \end{bmatrix} \frac{d}{dt} \begin{Bmatrix} \underline{u} \\ \underline{p} \\ \underline{T} \end{Bmatrix} = \begin{Bmatrix} \underline{f}_u \\ \underline{f}_p \\ \underline{f}_t \end{Bmatrix}$$

This system can be re-written as:

$$\underline{\underline{A}}\,\underline{x} + \underline{\underline{B}}\frac{d\underline{x}}{dt} = \underline{F}$$

and can be solved using a single-step finite difference operator such as in Lewis and Schrefler (1998) or Zienkiewicz and Taylor (2000).

4. NUMERICAL IMPLEMENTATION/ANALYSIS

The governing system of equations introduced in the previous section was solved using a C++ "in-house" finite element code. Preliminary investigations have been carried out on a 2D benchmark problem and a 2D EGS heat exchange volume. The EGS simulations show the potential capabilities of solving the fully coupled EGS heat exchange problem in a realistic poroperm medium. The numerical implementation is not complete in its current state. The details of future work and capabilities are important and will be discussed in Section 5.

Table 1 shows the material parameters used in this work. The parameters are taken to be an approximation for an EGS volume from parameters given in the SUTRA user's manual, Ingebritsen, et al. (2006), and Lewis and Schrefler (1998). These parameters and boundary conditions compose a representative parameter space intended demonstrate the potential capabilities of the FE code. More simulations will be run with more appropriate boundary conditions and material parameters in the future. Note that porosity and permeability are taken to be constants in the table. The constant presented is the mean value of data that fluctuates with $1/k$ spatial correlation sometimes called "pink noise." This is consistent with the spatial fluctuation in well-log data in most EGS volumes. Observed well-log and well-core spatial variation about the mean is of order ~ 5%-10%. For permeability, it is understood that this fluctuation magnitude applies to the logarithm of permeability, hence leading to substantially greater variation of permeability *per se*.

Table 2: Input Material Properties

Symbol	Parameter	Value	Units
E	Young's modulus	72.9	Gpa
ν	Poisson's ratio	0.14	-
β_s	solid coefficient of thermal expansion	5.50E-07	1/°C
ρ_s	solid density	2600	kg/m^3
ρ_w	fluid density	1000	kg/m^3
S_w	fluid saturation	1	-
n	porosity	0.2	-
C_s	solid specific heat	840	J/kg °C
C_w	fluid specific heat	4182	J/kg °C
σ_s	solid thermal conductivity	3.5	J/s m °C
σ_w	fluid thermal conductivity	0.6	J/s m °C
μ_w	fluid viscosity	0.0002	kg/m s
κ	permeability	1.00E-12	m^2
β_w	fluid coefficient of thermal expansion	2.02E-04	1/°C

4.1 Benchmarking Procedures

No analytical solutions to this coupled problem exist. To ensure that the code developed is working properly, the results can be compared to those presented in Lewis and Schrefler (1998) and Aboustit, et al. (1985). Both report the results of the same non-isothermal fully-saturated soil column consolidation problem. It is rather difficult to offer a direct comparison between the two problems because some of the material parameters used in this formulation are combined into "effective" parameters in the benchmark problem presented by the authors and it is not possible to exactly replicate their parameter space from the data they present. However, we will show that the trends in behavior are the same even with realistic EGS field parameters and in investigations not shown here, it is possible to reproduce the trends seen in Lewis and Schrefler (1998) by adjusting the material parameters.

Figure 2 displays the mesh used in the benchmark consolidation problem for this work. The bottom surface of the geometry is fixed in the vertical direction, while the sidewalls are fixed from displacement in the horizontal direction. The top surface has a prescribed traction of 1000 Pa applied, where the temperature is fixed at 50° C and the pore fluid pressure is set to be 0 Pa. The rest of the domain boundaries are fully insulated and sealed. In the outputs, we will analyze nodal values of displacement, pore fluid pressure, and temperature along all the nodes along the right sidewall boundary. The results are fully symmetric in the 2D (effectively 1D) problem, so either sidewall could be analyzed.

Figure 2: Benchmark mesh for non-isothermal consolidation problem. Adapted from (Aboustit, et al., 1985).

In accordance with the discussion from Lewis and Schrefler (1998), the matrices $\underline{\underline{R}}$ and $\underline{\underline{K}}_{tt}$ were set to zero. This means that temperature changes are not deemed to have a significant impact on the deformation state of the material and the coupling of the pore fluid pressure to changes in temperature are also small compared to the rest of the effects. This may be true for the material parameter space chosen in the work of Aboustit, et al. (1985), but for realistic parameter spaces at EGS depths, this simplification should not be allowed.

Figure 3 displays the displacement (consolidation) response of the medium from Lewis and Schrefler (1998) and Figure 4 displays the consolidation result from this work. The magnitudes of the displacements are not important, since different choices of material parameters can affect this. Even the signs of the displacement can be affected by the parameters associated with the coupling matrices. It is possible to reproduce these magnitudes and even the peak displacement before consolidation by adjusting the parameter space. However, Lewis and Schrefler (1998)

report that this peak disappears when realistic values for the bulk moduli are used (as in this work as seen in Figure 4).

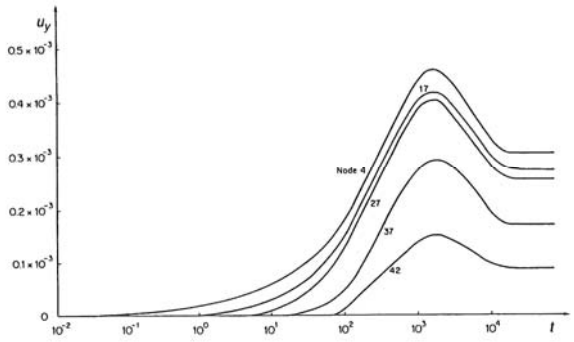

Figure 3: Vertical displacement values for different nodes in benchmark problem, taken from Lewis and Schrefler (1998).

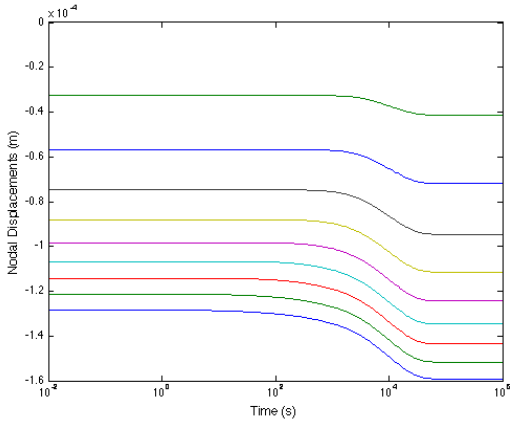

Figure 4: Vertical displacement of different nodes for soil consolidation problem from this work.

Figure 5 displays the pore fluid pressure evolution as a function of time from Lewis and Schrefler (1998). Figure 6 shows the results of the same plot from this work. These trends are identical. It is not clear if the pressures have been normalized in Figure 5. An interesting observation of Figure 5 is also that only 3 nodal values have been reported. This is most probably due to the oscillatory behavior of the pressure solution. Figure 6 shows the result of pressure for every node in the vertical direction and the oscillations are obvious, especially at early times. Both Aboustit et al. (1985) and Lewis and Schrefler (1998) report these oscillations in normalized data and they are apparent in these simulations as well. The oscillations are significantly reduced with the use of Babuska-Brezzi elements and mesh refinement. The trends in pore fluid pressure are identical to those shown in the benchmark problem presented by Lewis and Schrefler (1998).

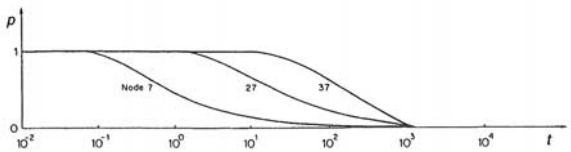

Figure 5: Pore fluid pressures for benchmark problem taken from Lewis and Schrefler (1998).

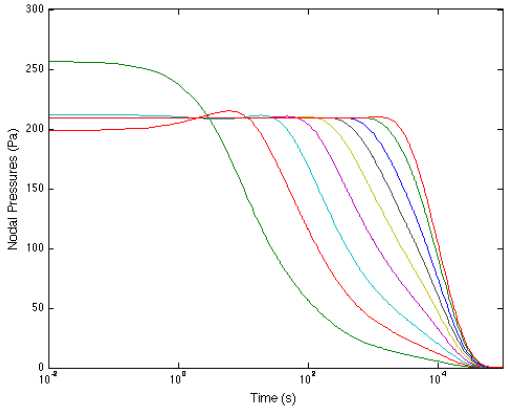

Figure 6: Evolution of pore fluid pressures from this work.

Figure 7 displays the nodal values of temperature over time from Lewis and Schrefler (1998) and Figure 8 displays the same variable from this work. Again, the exact trends are matched with the current model. The data of Figure 7 appear stretched compared to Figure 8, however, this is again due to the material parameter space. Adjustment of material parameters can give rise to the behavior seen in Figure 7.

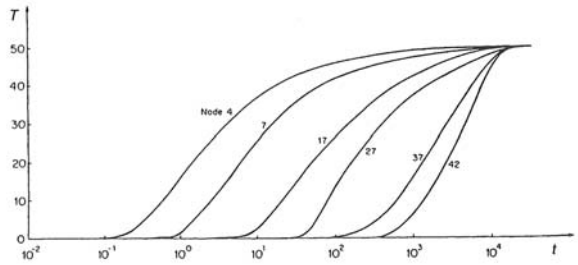

Figure 7: Nodal temperature evolution for benchmark problem taken from Lewis and Schrefler (1998).

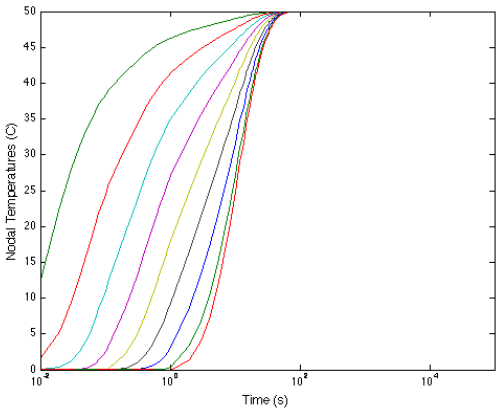

Figure 8: Evolution of nodal temperatures in this work.

Comparing Figure 4 to Figures 6 and 8 offers interesting insight into the displacement behavior of the column. The problem is formulated to be quasi-static. Therefore, the system should be in static equilibrium at each time step. When a compressive traction load is placed on the top surface of the column, the column is compressed uniformly

near to the linear elastostatic solution. Figure 4 shows this result even at very small times. However, after pressure and temperature have roughly equilibrated, there is a noticeable consolidation effect on the column as the displacements further decrease. This result makes sense from a solid mechanics perspective, because pore pressure can be thought of as incompressibility in the medium. As the pressure is decreased, the magnitude of the displacements should increase. This is clearly demonstrated in Figure 4.

To demonstrate the importance of the matrices $\underline{\underline{R}}$ and $\underline{\underline{K}}_{tt}$ when realistic material parameters for EGS volumes are used, the terms were included in the results generating the data of Figure 9. The figure displays the displacement behavior of the column in that case.

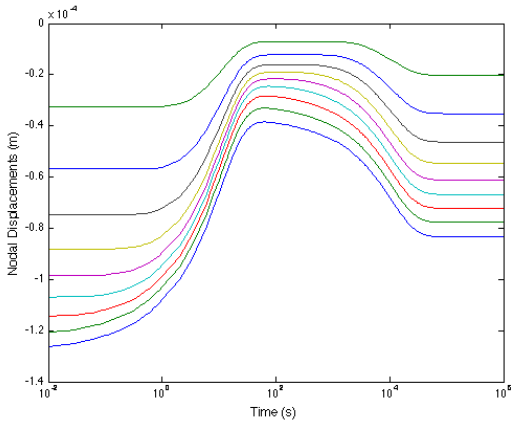

Figure 9: Displacement evolution for fully coupled problem with appropriate EGS parameters.

4.3 Double Borehole Simulation Set-up

Figure 10 displays the double borehole simulation set up. The figure is colored by the porosity, which varies spatially with 1/k correlation. The domain size is 70 m wide by 40 m tall with 0.5 m borehole widths. The horizontal distance between the boreholes is 14 m. The external boundary is fixed with temperature set to 200°C and pore fluid pressure set to 2 MPa. 100°C fluid flows into the left borehole that is pressurized to 4 MPa. The simulation was performed with time steps of 500.0 s to a final time of 7000 s to reach equilibrium.

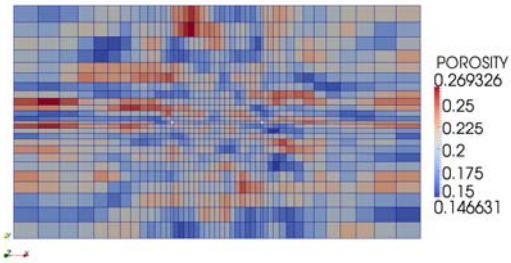

Figure 10: Double borehole simulation mesh and porosity.

4.4 Double Borehole Preliminary Simulation Results

Figures 11 and 12 display the results for the primary variables of pore fluid pressure and temperature in the double bore simulations.

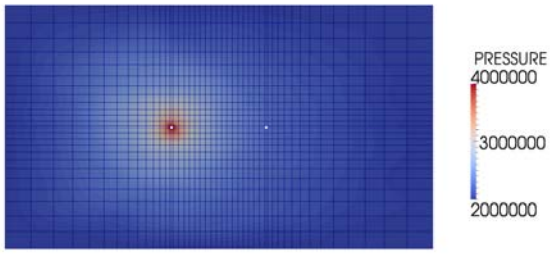

Figure 11: Double borehole pore fluid pressure.

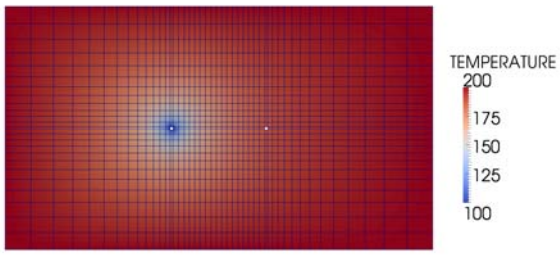

Figure 12: Double borehole domain temperature.

Figure 13 displays the result for shear stress in the double borehole simulations. Underground fractures often occur in regions of maximum shear stress. Therefore, shear stress in the domain could be used in future work incorporating an increase in fracture density.

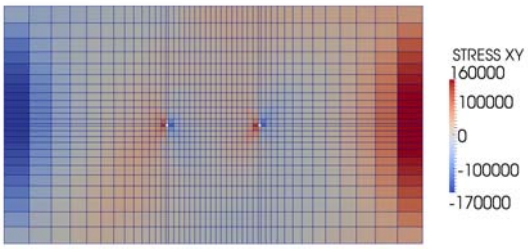

Figure 13: Double borehole shear stress.

Figure 14 displays the result for the magnitude of the fluid velocity. There is a greater fluid velocity around the pressurized borehole. However, the fluid velocity is not symmetric. This is due to differences in porosity and permeability around the borehole. The higher porosity results in a lower velocity on the left side of the borehole. This may result in a greater overall flow in that direction, but the outflow calculations have not yet been implemented into the C++ FE code.

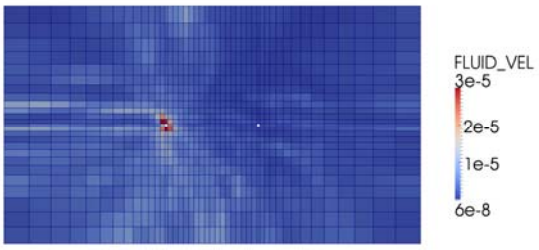

Figure 14: Double borehole magnitude of fluid velocity.

5. DISCUSSION/CONCLUSIONS

5.1 Results

The results in Section 4 are preliminary results intended to demonstrate potential modeling capabilities of FE codes applied to coupled thermo-poro-mechanical processes in realistic heterogeneous media such as EGS rock volumes. While the meshes represent relatively small domains and have very coarse levels of refinement, the physics of EGS flow is implemented and the potential exists to offer new insight into the understanding of *in situ* fluid flow, heat transport, and pressure-induced fracture evolution.

It is imperative for long-term energy solutions that the coupled physics of EGS volumes are well understood. Simulations of this type and Figures 10-14 allow for the comparison of material and domain characteristics to resulting fluid flows and, potentially, fracture networks. Figure 14 clearly depicts fluctuations in small fluid velocities that are dependent upon the values of porosity and permeability within the domain. The temperature at a receiver well is important to consider as well as the outflow. From Figure 12, the temperature surrounding the outflow wellbore is about 180° C.

5.2 Future Work

There is a significant amount of future work to perform for EGS simulations that used the C++ code from this work. It is highly desirable to determine the exact fluid mass outflow at boundaries (i.e., outflow wellbore boundaries). Taking the dot product of Darcy's Law for fluid and the boundary of interest's outward normal vector performs this calculation. This implementation is straightforward, but requires the robust and consistent determination of the outward normal vector at a boundary.

As mentioned in Section 2, the temperature dependence of certain fluid properties (e.g., density and viscosity) needs to be accounted for. Over the range of these simulations (100-200°C), a linear dependence in fluid density is not a bad assumption. However, more complicated relationships can easily be incorporated into the code. Constant water viscosity at 200°C was used in the borehole simulations of Section 4. Figure 15 displays water viscosity as a function of temperature. Like fluid density, it is straightforward to implement a temperature dependence of the fluid viscosity term into the code assuming that no fluid phase changes are present within the simulation.

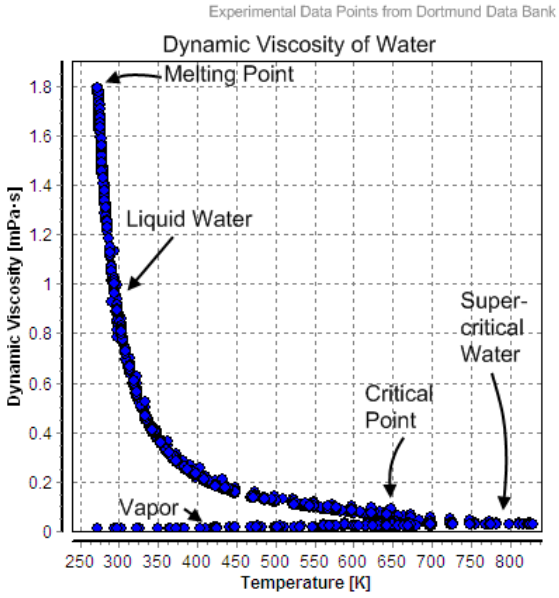

Figure 15: Temperature dependence of water viscosity.

Solving for the stresses and strains in the domain allows for more robust consideration of fracture networks. Natural pathways for fluid flow (fracture networks) already exist in EGS volumes. These systems can be enhanced by borehole pressurization through an influx of fluid. The enhancement of natural fracture networks will be explored in this work. A working hypothesis indicates that when critical stresses or strains are reached within a portion of the domain, permeability and porosity in that portion of the domain will increase appropriately as a result of an increase in fracture density. This can allow for fluid flows to also increase appropriately in highly stressed regions.

Further, these 2-dimensional analyses will be extended to 3 dimensions for more complete representation of geothermal fields. This extension will require significantly more computational cost. The problems presented here already require a computational cost that is not insignificant. It was mentioned in Section 5 that these are relatively coarse meshes; therefore the simulations are relatively small. Memory availability limits the maximum size problems that can be computed. It is imperative for future work to implement the FETI method for parallel computation in finite element analysis on a MPI cluster located at the University of Auckland. Parallelization will allow for faster run time of large simulations as well as reduced memory requirements for individual CPUs. This will allow for full-scale 3-D simulations with significantly refined mesh structures.

REFERENCES

Aboustit, B.L., Advani, S.H., and Lee, J.K., Variational Principles and Finite Element Simulations for Thermo-elastic Consilidation, *International Journal for Numerical and Analytical Methods in Geomechanics.* 9, pp 49-69 (1985).

Goldstein, B.A., Hiriart, G., Tester, J., B., Bertani, R., Bromley, Gutierrez-Negrin, L.,C.J., Huenges, E., H, Ragnarsson, A., Mongillo, M.A. Muraoka, and V. I. Zui, Great expectations for geothermal energy to 2100, *Proceedings Thirty-Sixth Workshop on Geothermal Reservoir Engineering*, Stanford University, Stanford, California, January 31 - February 2, 2011

Hughes, T.J.R.: *The Finite Element Method: Linear Static and Dynamic Finite Element Analysis.* Dover Publications. (2000).

Ingebritsen, S., Sanford, W., and Neuzil, C.: *Groundwater in Geologial Processes*. pp. 1 - 155. Cambridge University Press. (2006).

Leary, P.C. Fractures and physical heterogeneity in crustal rock, in *Heterogeneity of the Crust and Upper Mantle – Nature, Scaling and Seismic Properties,* J. A. Goff, & K. Holliger (eds.), Kluwer Academic/Plenum Publishers, NewYork, 155-186, (2002) .

Leary, P.C. and Walter, L.A.: Crosswell Seismic Applications to Highly Heterogenous Tight Gas Reservoirs. *First Break* 26 (2008).

Lewis, R.W. and Schrefler, B.A.: *The Finite Element Method in the Static and Dynamic Deformation and Consolidation of Porous Media*. pp. 9 - 97, 341 - 394. John Wiley and Sons. (1998).

Sutter, D., Fox, D.B., Anderson B.J., Koch. D.L., Rudolf von Rohr, P., Tester, J.W., Sustainable heat farming of geothermal systems: a case study of heat extraction and thermal recovery in a model EGS fractured reservoir, *Proceedings Thirty-Sixth Workshop on Geothermal Reservoir Engineering*, Stanford University, Stanford, California, January 31 - February 2, 2011

Zienkiewicz, O.C. and Taylor, R.L.: *The Finite Element Method: Volume 1 – The Basis. 5th Edition.* Butterworth and Heinemann. (2000).